# Sparse Deconvolution of Electrodermal Activity via Continuous-Time System Identification

Md. Rafiul Amin, *Student Member, IEEE,* Rose T. Faghih, *Member, IEEE*

***Abstract*—*Objective:*** **Electrodermal activity (EDA) indicates different eccrine sweat gland activity caused by the stimulation of the autonomic nervous system. Recovering the number, timings, and amplitudes of underlying neural stimuli and physiological system parameters from EDA is a challenging problem. One of the challenges with the existing methods is the non-convexity of the optimization formulations for estimating the parameters given the stimuli.** ***Methods:*** **We solve this parameter estimation problem using a continuous-time system identification framework: i) We specifically use the Hartley modulating function (HMF) for parameter estimation so that the optimization formulation for estimating the parameters given the stimuli is convex; ii) We use Kaiser windows with different shape parameters to put more emphasis on the significant spectral components so that there is a balance between filtering out the noise and capturing the data. We apply this algorithm to skin conductance (SC) data, a measure of EDA, collected during cognitive stress experiments.** ***Results:*** **Under a sparsity constraint, in the HMF domain, we successfully deconvolve the SC signal. We obtain number, timings, and amplitudes of the underlying neural stimuli along with the system parameters with $R^2$ above 0.915. Moreover, using simulated data, we illustrate that our approach outperforms existing EDA data analysis methods, in recovering underlying stimuli.** ***Conclusion:*** **We develop a novel approach for deconvolution of SC by employing the HFM method and capturing the significant spectral components of SC data.** ***Significance:*** **Recovering the underlying neural stimuli more accurately using this approach will potentially improve tracking emotional states in affective computing.**

***Index Terms*—Biomedical signal processing, optimization, deconvolution, system identification, state-space methods**

## I. Introduction

In general, electrodermal activity (EDA) refers to any changes in the electrical characteristics of skin due to different physiological activities. Skin conductance response (SCR), which is one of the measures of EDA for physiological analysis, indicates different eccrine sweat gland activities caused by the stimulation of autonomic nervous system (ANS), mainly by sudomotor nerve [1]. When sweat secretions occur in response to stimulations from the autonomic nervous system, there is an alteration in the ionic permeability of the cell membranes. This change in permeability increases conductance in skin tissue. Although sweating, controlled by hypothalamic areas, is mostly intended for thermoregulation, it also depends on other physiological events including emotional arousal [2]. Many works attest to the high correlation between sympathetic nervous activity and EDA [3], [4].

This work was supported in part by NSF 1755780. Md. Rafiul Amin and Rose T. Faghih are with the University of Houston, Houston, TX, 77204-4005 USA (e-mail: mamin@uh.edu, rtfaghih@uh.edu)

Physiological signals like EDA that have a high correlation with sympathetic nervous activity can help to interpret emotional dysfunctions or abnormalities. Emotional dysfunctions influence psychiatric disorders like depression [5]. Many studies have shown risks of suicidal behavior in patients having psychiatric disorders including depression and posttraumatic stress disorder [6], [7], [8]. Mortality due to mental disorders has been identified as one of the major causes of death worldwide [9]. Moreover, dysregulation in arousal can cause symptoms including insomnia and irritability [10]. Patients with posttraumatic stress disorder show symptoms of difficulty in falling asleep and excessive irritability [11]. In psychopathology, identifying problematic patterns of emotion and emotional regulation can characterize psychiatric disorders [12], [13]. Several studies have been carried out to detect mental disorders using emotional tracking [14] and from disturbed arousal conditions [15]. Mental disorder-related issues could be significantly reduced if a personalized health monitoring system [16] with a user-friendly daily psychological condition tracking could be devised.

Macefield *et al.* [14] have shown that areas of the brain related to sympathetic nervous activity can be identified by using functional magnetic resonance imaging (fMRI) of the brain and by recording concurrent microelectrodes readings generated by sympathetic outflow to muscle and skin. They have proposed to extend this idea to examine specific disorders of emotional expression to comprehend underlying neural processes. To collect fMRI data, a clinical setup is necessary which will be convenient for clinical diagnosis. Unfortunately, it is not convenient for daily tracking of neural process related to emotional states. Bomba *et al.* [17] used heart rate variability (HRV) from the ECG signal as a measure of ANS imbalance. However, Soh *et al.* [18] illustrated the underlying challenges and complexity of acquiring ECG data using wearable technology. In another study, Faghih *et al.* [19] were able to recover the amplitude and timing of neural stimuli related to different fear states employing EDA signals with a deconvolution scheme [20], [21]. Utilizing recovered timings and amplitudes, emotional states can be estimated to analyze emotional disorders.

Many deconvolution schemes have been proposed for physiological signals including skin conductance (SC) data. Benedek *et al.* [22] proposed a non-negative approach to decompose SC data into discrete compact responses and at the same time assessed deviations from the standard SCR shape. However, this decomposition approach could detect noise as SCR and does not include the individual differences in modeling the fall and rise times. Greco *et al.* [23] proposed

decomposing SC data into tonic and phasic components. They formulated a quadratic programming problem to find sparse solutions for the input stimuli. However, the use of fixed regularization parameter makes it challenging to find an optimal sparse solution. In another work, Gallego *et al.* [24] proposed an approach to obtain a more sparse solution; however, this approach seems to oversparsify the solution. In the deconvolution scheme proposed by Faghih *et al.* [25], [19], [20], [21], [26], a two-step coordinate descent approach has been incorporated. In the first step, they used the FOCal Under-determined System Solver (FOCUSS) algorithm [27] to find a sparse solution of the neural stimuli. This step is a convex optimization problem to which a global solution can be achieved. In the following step, their algorithm employs another optimization problem to find the physiological system parameters, which is not convex. Therefore, it is possible for the solution to stagnate at a local minimum.

In the present study, we propose an algorithm to find neural stimuli and underlying system parameters and use this algorithm to analyze EDA data. Inspired by the work carried out by Faghih *et al.* [25], [19], [20], [21], [26], we use a state-space model to relate SC with internal unobserved neural stimuli. However, in this work, we re-formulate the optimization problems for model parameter estimation in [25], [19], [20], [21], [26] as a convex problem to avoid stagnation of the solutions at local minima. In contrast to the model proposed in [19], we only model the phasic component of SC as a state variable in our state-space equations. We separate the phasic component from the SC using the cvxEDA algorithm proposed in [23]. Then, we take a coordinate descent approach to recover the neural stimuli and estimate the system parameters. We use a modified version of FOCUSS [20] to solve the inverse problem of finding neural stimuli from SC data. For system parameters estimation, we employ a continuous-time system identification approach using Hartley Modulating function. This allows for formulating this problem as a convex optimization problem in terms of neural stimuli and physiological system parameters. We also incorporate a data dependent bandwidth selection approach for more accurate estimation of physiological system parameters. Then, we apply our method to analyze SC data collected during cognitive stress tasks. We successfully recover underlying stimuli and the physiological parameters.

## II. Methods

### A. Experiment

*1) Dataset 1:* In this study, we analyze publicly available dataset collected by Quality of Life Laboratory at the University of Texas at Dallas [28]. The data was collected from 20 college students. Fourteen of them were male and six of them were female. Information on subject ID, age, gender and body mass index (BMI) of each subject are provided in the supplementary information. The experiment was carried out to distinguish between physiological signals during different types of stresses ('cognitive stress', 'emotional stress', 'physical stress' and 'relaxing'). A detailed explanation of the experiment is given in [28]. In this study, we analyze EDA data from 3-minute 'counting task' of the 'cognitive stress' portion of the study. In the 'counting task', the subjects have to count backwards by sevens, beginning with 2485, for three minutes. The SC signal was measured with a sampling frequency of 8 Hz. In our study, we downsample the data by a factor of 2 and obtain the 4Hz signal for analysis. Further, we discard all the signals that have been corrupted by heavy artifacts. Therefore, we only analyze 6 subjects whose SC signals are not corrupted by heavy motion artifacts.

*2) Dataset 2:* Skin conductance responses to loud sounds, simultaneously recorded from palm, fingers and foot [29] dataset were collected for modeling event-related SC responses. Participants were asked to press a foot operated pedal in response to 20 auditory stimuli. Auditory stimulations are one-second long white noise bursts. The details of the experiment are in [30]. We use SC recordings from the middle phalanx of the dominant second and third finger for our study. The dataset contains the timings of the auditory stimulations to perform the comparison with the recovered stimuli. We use this dataset to perform the comparison with existing methods. The signals in this dataset have a sampling frequency of 100 Hz. We downsample the data to 4 Hz for our analysis.

### B. Model Formulation

The SC data can be represented as a summation of two different signals [22], [31]. One is a slowly varying signal called tonic component and another is a comparatively fast varying signal called phasic component. We separate the phasic component from SC using the algorithm proposed by Greco *et al.* [23].

The phasic component of the SC can be modeled as a second order differential equation. We use a second order differential equation model similar to the models in [19], [31]. This model describes the changes in the phasic SC as a function of the activity of the sudomotor nerve. The model is defined in state-space form as follows:

$$\dot{x}_1(t) = -\frac{1}{\tau_1}x_1(t) + \frac{1}{\tau_1}u(t) \tag{1}$$

$$\dot{x}_2(t) = \frac{1}{\tau_2}x_1(t) - \frac{1}{\tau_2}x_2(t) \tag{2}$$

where $x_2$ is the SC level of the phasic component and $x_1$ is an internal unobserved state variable. $\tau_1$ and $\tau_2$ are SC time constants in the model corresponding to the rise time and fall time, respectively. This time-invariant system representation can model the phasic responses under the assumption that the time constants $\tau_1$ and $\tau_2$ do not change over the duration of the experiment. It is known that a single neural impulse from ANS is responsible for a single phasic SC response [32], [24], [19]. The length of the experimental signals and average separation of the consecutive phasic SC responses are very high compared to the number of the neural stimuli generated by ANS; hence, we can include a sparsity constraint on the neural stimuli. In contrast to the model proposed in [31], we consider a finite number of stimuli as the model input (similar to [32], [24], [19]). This definition makes it suitable to take timings and amplitudes of the stimuli to quantify emotional states. We define the sparse abstraction of the input stimulation as $u(t) = \sum_{i=1}^{N} q_i \delta(t - \Delta_i)$, where $q_i$ represents the level of

stimulation at time $\Delta_i$. $q_i$ of zero implies no stimulation at time $\Delta_i$. $N$ refers to the length of the input; $N$ is a function of the duration of the experiment and the input sampling interval $T_u$. In this case, we can write $\Delta_i = iT_u$.

*1) Discrete-Time System Identification:* Let's say the signal has been sampled with a sampling interval of $T_y$ for $M$ samples. We can define the observed phasic SC data $y_{t_k}$ as follows:

$$y_{t_k} = x_2(t_k) + \nu_{t_k} \tag{3}$$

where $k = 1, 2, \cdots, M$; $t_k = kT_y$ and $\nu_{t_k}$ represents signal noise. We model $\nu_{t_k}$ as a Gaussian random variable and use this assumption to implement a least squares approach in our estimation algorithm. Using the phasic SC data $y_{t_k}$, we would like to estimate $\tau_1$ and $\tau_2$, and also recover the input $u(t)$, i.e., amplitude and timing of the stimuli. Assuming that $x_1(0) = 0$, solution for $y_{t_k}$ would be as follows:

$$y_{t_k} = a_{t_k} y_0 + \mathbf{b}_{t_k}\mathbf{u} + \nu_{t_k} \tag{4}$$

where $a_{t_k} = e^{-\frac{t_k}{\tau_2}}$, $\mathbf{b}_{t_k} = \big[\frac{1}{(\tau_1-\tau_2)}(e^{-\frac{t_k}{\tau_1}} - e^{-\frac{t_k}{\tau_2}})$ $\frac{1}{(\tau_1-\tau_2)}(e^{-\frac{t_k-T_u}{\tau_1}} - e^{-\frac{t_k-T_u}{\tau_2}})$ $\frac{1}{(\tau_1-\tau_2)}(e^{-\frac{t_k-2T_u}{\tau_1}} - e^{-\frac{t_k-2T_u}{\tau_2}})$ $\cdots$ $\frac{1}{(\tau_1-\tau_2)}(e^{-\frac{T_u}{\tau_1}} - e^{-\frac{T_u}{\tau_2}})$ $\underbrace{0 \quad \cdots \quad 0}_{N-\frac{t_k}{T_u}}\big]$ and vector $\mathbf{u} = [q_1 \quad q_2 \quad \cdots \quad q_N]^\top$ represents the entire input over the entire experiment. Let $\mathbf{y} = [y_{t_1} \quad y_{t_2} \quad \cdots \quad y_{t_M}]^\top$, $\boldsymbol{\tau} = [\tau_1 \quad \tau_2]^\top$, $\mathbf{A}_\tau = [a_{t_1} \quad a_{t_2} \quad \cdots \quad a_{t_M}]^\top$, $\mathbf{B}_\tau = [\mathbf{b}_{t_1} \quad \mathbf{b}_{t_2} \quad \cdots \quad \mathbf{b}_{t_M}]^\top$, $\boldsymbol{\nu} = [\nu_{t_1} \quad \nu_{t_2} \quad \cdots \quad \nu_{t_M}]^\top$ and $y_0$ is the initial condition of the phasic SC level. Here, $T_y$ is always an integer multiple of $T_u$. Now we can represent the system as:

$$\mathbf{y} = \mathbf{A}_\tau y_0 + \mathbf{B}_\tau \mathbf{u} + \boldsymbol{\nu}. \tag{5}$$

(5) shows the representation of the sampled phasic SC data. In this study, we simulate data using a state-space approach. A detailed description is given in the supplementary information. In this study, we are considering $T_u = T_y$ and $N = M$, i.e., we take the resolution of input vector $\mathbf{u}$ as same as $\mathbf{y}$.

*2) Continuous-Time System Identification:* In continuous-time system identification technique, we transform the signal into a new domain according to the system model so that the optimization problem for finding system parameters $\tau_1$ and $\tau_2$ becomes convex. We first write the two first-order coupled differential equations ((1)-(2)) as a second-order differential equation:

$$\alpha_2 \frac{\mathrm{d}^2 y(t)}{\mathrm{d}t^2} + \alpha_1 \frac{\mathrm{d}y(t)}{\mathrm{d}t} + y(t) = u(t) \tag{6}$$

where $y(t)$ is the continuous equivalent of $y_{t_k}$, $\alpha_1 = \tau_1 + \tau_2$, and $\alpha_2 = \tau_1\tau_2$. If we find $\alpha_1$ and $\alpha_2$, then we can solve for $\tau_1$ and $\tau_2$. Let $\boldsymbol{\Theta} = \begin{bmatrix} \alpha_1 & \alpha_2 \end{bmatrix}^\top$, $g_0(\boldsymbol{\Theta}) = (\alpha_2^2 - 4\alpha_1)$. Hence:

$$\boldsymbol{\tau} = \mathbf{g}(\boldsymbol{\Theta}) = \begin{bmatrix} g_1(\Theta) \\ g_2(\Theta) \end{bmatrix} = \begin{bmatrix} \frac{1}{2}\left(\alpha_1 - \sqrt{g_0(\boldsymbol{\Theta})}\right) \\ \frac{1}{2}\left(\alpha_1 + \sqrt{(g_0(\boldsymbol{\Theta})}\right) \end{bmatrix}. \tag{7}$$

The modulating function method for identifying the model parameters begins with multiplying both sides of (6) by the modulating function and integrating over $T_d$, which is the duration of the sampled signal. The modulating function is given by $\phi_m(t)$ where the integer $m$ refers to the $m^{\text{th}}$ spectral component. The length of the modulating function is chosen as same as the sampling duration of the signal. The integration results in

$$\alpha_2 \int_0^{T_d} \phi_m(t) \frac{\mathrm{d}^2 y(t)}{\mathrm{d}t^2} dt + \alpha_1 \int_0^{T_d} \phi_m(t) \frac{\mathrm{d}y(t)}{\mathrm{d}t} dt + \int_0^{T_d} \phi_m(t) y(t) dt = \int_0^{T_d} \phi_m(t) u(t) dt. \tag{8}$$

### C. Estimation

To accomplish our goal, we break down the problem into two sub-problems. One is to find the model parameters $\boldsymbol{\tau}$ and another is the inverse problem, i.e., to find the stimuli $\mathbf{u}$. Inspired by the coordinate descent deconvolution scheme by Faghih *et al.* [20], we follow a similar approach. Unlike [20], we use a continuous system identification approach for the parameter estimation. Then, we solve the inverse problem using the FOCUSS algorithm [27]. Using a coordinate descent approach, we iterate between these two steps until convergence. These two steps are described in detail in Sections II-C1 and II-C2. Then, the coordinate descent approach is discussed in Section II-C3.

*1) System Identification using Hartley Modulating Functions:* There are different modulating functions that could be used for continuous-time system identification. One can use any modulating function according to their convenience [33], [34]. Among the two most widely used modulating functions, one option is the Fourier modulating function [34]; however, it involves complex values and is not the best choice for this study. Another one is the Hartley modulating function (HMF) which does not involve complex numbers in spectral components. Apart from having real coefficients, this modulating function also does not depend on the boundary conditions and the computations of all the spectral components can be made using fast algorithms for the discrete Hartley transformation [35]. We use the HMF approach as this function and its corresponding spectral components are always real-valued and yet contain all the information contained in the Fourier modulating function [33], [34]. For a $\kappa^{\text{th}}$ order system, the $\kappa^{\text{th}}$ order HMF spectral component has to be calculated. The properties of a $\kappa^{\text{th}}$ order HMF allow us to formulate a convex optimization formulation for model parameter estimation.

***Properties of HMF:*** The $\kappa^{\text{th}}$ order HMF [35] with fixed time interval $[0, T_d]$ is as follows:

$$\phi_m(t) = \sum_{j=0}^{\kappa} (-1)^j \binom{\kappa}{j} \mathrm{cas}((\kappa + m - j)\omega_0 t) \tag{9}$$

where for a variable $s$, $\mathrm{cas}(s) = \cos(s) + \sin(s)$ and $\frac{\mathrm{dcas}(s)}{\mathrm{d}s} = \mathrm{cas}(-s)$. HMF $\phi_m(t)$ has the following properties:

$$\begin{gathered} \phi_m(t) \text{ is zero beyond the interval } [0, T_d], \\ \text{the } l^{\text{th}} \text{ derivative } \phi_m^{(l)}(t) \text{ exists for all } l = 0, 1, \cdots, \kappa - 1 \text{ and} \\ \phi_m^{(m)} = 0 \text{ for } t = 0 \text{ and } t = T_d \end{gathered} \tag{10}$$

where $\omega_0 = \frac{2\pi}{T_d}$. In this study, the model order is 2. Since we are given the sampled signal, we repeatedly apply integration-by-parts in (8) until all derivatives of input (or output) signal vanish. For any signal $\zeta(t)$, the $\kappa^{\text{th}}$ order spectral component of $l^{\text{th}}$ derivative of the signal can be written as below [36], [37]:

$$\bar{H}_{\zeta}^{(l)}(m\omega_0) = \int_0^{T_d} \phi_m(t)\frac{\mathrm{d}^l\zeta(t)}{\mathrm{d}t^l}dt = \sum_{j=0}^{\kappa}(-1)^j\binom{\kappa}{j}(\kappa+m-j)^l \cdot \omega_0^l \mathrm{cas}(-\frac{l\pi}{2})H_{\zeta}((-1)^l(\kappa+m-j)\omega_0) \tag{11}$$

where $\bar{H}_{\zeta}^{(l)}(m\omega_0)$ is the $m^{\text{th}}$ HMF spectral component of $l^{\text{th}}$ derivative of the continuous signal $\zeta(t)$, and $H_{\zeta}(\omega)$ is the Hartley Transform (HT) [38] of $\zeta(t)$ defined by,

$$H_{\zeta}(\omega) = \int_{-\infty}^{\infty}\zeta(t)\mathrm{cas}(\omega t)dt. \tag{12}$$

Its corresponding transformation of discrete sequence with $N_{\zeta}$ samples and duration $T_d$ is given by,

$$\hat{H}_{\zeta}(m) = \frac{1}{N_{\zeta}}\sum_{\eta=0}^{M-1}\zeta\left(\frac{\eta T_d}{N_{\zeta}}\right)\mathrm{cas}\left(\frac{2\pi m\eta}{N_{\zeta}}\right)dt. \tag{13}$$

Estimation of HMF spectral components can be carried out using continuous Hartley transform with numeric integration using (12) or direct estimation of Hartley transform using (13). In this study, we use (12) and trapezoidal rule for the numeric integrations for Hartley transform. The number of samples $N_{\zeta}$ for signal $y(t)$ and $u(t)$ is equal to $M$ and $N$, respectively.

*Convex Cost Function Formulation with Linear Regression :* Using (11), we can rewrite (8) as,

$$\alpha_2\bar{H}_y^{(2)}(m\omega_0) + \alpha_1\bar{H}_y^{(1)}(m\omega_0) = -\bar{H}_y^{(0)}(m\omega_0) + \bar{H}_u^{(0)}(m\omega_0). \tag{14}$$

Here,

$$\begin{aligned}\bar{H}_u^{(0)}(m\omega_0) &= \int_0^{T_d}\phi_m(t)u(t)dt = \int_0^{T_d}\phi_m(t)\sum_{i=1}^{N}q_i\delta(t-\Delta_i)dt \\ &= \sum_{i=1}^{N}\phi_m(\Delta_i)q_i \\ &= \underbrace{\begin{bmatrix}\phi_m(T_u) & \phi_m(2T_u) & \cdots & \phi_m(NT_u)\end{bmatrix}}_{b_{\phi}^{\top}(m\omega_0)}\begin{bmatrix}q_1\\q_2\\\vdots\\q_N\end{bmatrix} \\ &= b_{\phi}^{\top}(m\omega_0)\mathbf{u}.\end{aligned}$$

We can rewrite (14) as follows,

$$\bar{H}_y^{(0)}(m\omega_0) \quad = -\alpha_2\bar{H}_y^{(2)}(m\omega_0) - \alpha_1\bar{H}_y^{(1)}(m\omega_0) + b_{\phi}^{\top}(m\omega_0)\mathbf{u}. \tag{15}$$

Let $Z(m\omega_0) = \bar{H}_y^{(0)}(m\omega_0)$ and let $\varepsilon(m\omega_0)$ model the error in the new domain. Rearranging the (14), it can be rewritten as a linear regression,

$$Z(m\omega_0) = \Phi^{\top}(m\omega_0)\boldsymbol{\Theta} + b_{\phi}^{\top}(m\omega_0)\mathbf{u} + \varepsilon(m\omega_0) \tag{16}$$

where

$$\Phi^{\top}(m\omega_0) = -\begin{bmatrix}\bar{H}_y^{(2)}(m\omega_0) & \bar{H}_y^{(1)}(m\omega_0)\end{bmatrix}.$$

Taking a sequence of observation for $m = 0, \pm1, \pm2, \cdots, \pm\mathcal{M}$ where $\mathcal{M}$ is the maximum frequency component. Then, (16) can be rewritten as a vector equation. Hence, the following optimization problem can be formulated to find the parameter vector $\boldsymbol{\Theta}$, $\beta$ and $\mathbf{u}$:

$$\begin{aligned}\underset{\boldsymbol{\Theta},\mathbf{u},\beta}{\text{minimize}} \quad & J(\boldsymbol{\Theta},\mathbf{u},\beta) = \frac{1}{2}\boldsymbol{\varepsilon}^{\top}(\mathcal{M}\omega_0)\mathbf{W}(\beta)\boldsymbol{\varepsilon}(\mathcal{M}\omega_0) \\ \text{subject to} \quad & \\ & G(\boldsymbol{\Theta}) \le \mathbf{0} \\ & ||\mathbf{u}||_0 \ll N \\ & \mathbf{u} \ge \mathbf{0}\end{aligned} \tag{17}$$

where, $G(\boldsymbol{\Theta}) = \begin{bmatrix}-g_0(\boldsymbol{\Theta})\\ \tau_1^{min} - g_1(\boldsymbol{\Theta})\\ g_1(\boldsymbol{\Theta}) - \tau_1^{max}\\ \tau_2^{min} - g_2(\boldsymbol{\Theta})\\ g_2(\boldsymbol{\Theta}) - \tau_2^{max}\end{bmatrix}$, $\mathbf{W}(\beta)$ is positive-definite symmetric frequency dependent weighting matrix with the shape parameter $\beta$, $\boldsymbol{\varepsilon}(\mathcal{M}\omega_0) = \boldsymbol{Z}(\mathcal{M}\omega_0) - \boldsymbol{\Phi}(\mathcal{M}\omega_0)\boldsymbol{\Theta} - \boldsymbol{B}_{\phi}^{\top}(\mathcal{M}\omega_0)\mathbf{u}$,

$$\boldsymbol{\Phi}^{\top}(\mathcal{M}\omega_0) = \begin{bmatrix}\Phi(-\mathcal{M}\omega_0) & \cdots & \Phi(-\omega_0) & \\ \Phi(0) & \Phi(\omega_0) & \cdots & \Phi(\mathcal{M}\omega_0)\end{bmatrix},$$

$$\boldsymbol{B}_{\phi}^{\top}(\mathcal{M}\omega_0) = \begin{bmatrix}b_{\phi}(-\mathcal{M}\omega_0) & \cdots & b_{\phi}(-\omega_0) & \\ b_{\phi}(0) & b_{\phi}(\omega_0) & \cdots & b_{\phi}(\mathcal{M}\omega_0)\end{bmatrix}$$

and

$$\boldsymbol{Z}^{\top}(\mathcal{M}\omega_0) = \begin{bmatrix}Z(-\mathcal{M}\omega_0) & \cdots & Z(-\omega_0) & \\ Z(0) & Z(\omega_0) & \cdots & Z(\mathcal{M}\omega_0)\end{bmatrix}.$$

(17) is convex in terms of $\mathbf{u}$ and $\boldsymbol{\Theta}$ (please see the appendix information for the convexity proof). Given $\beta$ and $\mathbf{u}$, we can find $\hat{\boldsymbol{\Theta}}$ by minimizing the cost function defined in (17) considering physiological constraints on time constants $\tau_1$ and $\tau_2$ given by $\mathbf{G}(\boldsymbol{\Theta}) \le \mathbf{0}$. The first constraint restricts the solution of $\tau_1$ and $\tau_2$ to be real valued. In the second and third constraints, we assume rise time $\tau_1$ is within physiological lower and upper bounds $\tau_1^{min}$ and $\tau_1^{max}$, respectively. In the fourth and fifth constraints, We also assume fall time $\tau_2$ is within physiological lower and upper bounds $\tau_2^{min}$ and $\tau_2^{max}$, respectively. We assume $\mathbf{u}$ is sparse and hence contains very small number of non-zero elements out of $N$ possibilities ($||\mathbf{u}||_0 \ll N$). As $\mathbf{u}$ refers to the neural stimuli from the brain, all the elements of $\mathbf{u}$ are nonnegative ($\mathbf{u} \ge \mathbf{0}$). We solve this constrained optimization problem using the interior point method.

*Parameter $\mathcal{M}$ Selection for Maximum Frequency Component Inclusion:* The Parameter $\mathcal{M}$ has to be selected such that it captures the signal and yet cancels out the noise. Garnier *et al.* [39] recommend choosing $\mathcal{M}\omega_0$ close to the bandwidth of the system to be identified. We calculate the maximum bandwidth $\omega_{max}$ by plugging in the extreme values $\tau_1^{max}$ and $\tau_2^{max}$ in $\alpha_1$ and $\alpha_2$ parameters of (6) to get the transfer function and calculate the corresponding bandwidth. Then,

we let $\mathcal{M} = \frac{2\omega_{max}}{\omega_0}$. This choice of $\mathcal{M}$ allows for including all the required frequency components. In order to take the appropriate spectral components of any given data, we propose an adaptive procedure for choosing the weighting matrix $\mathbf{W}$ automatically.

*Choosing Weighting Matrix* $\mathbf{W}$*:* Many authors have suggested taking all the spectral components into account to include the maximum possible frequency component of the system [37], [40]. However, according to our investigation that does not work well for our deconvolution scheme. Sometimes, it captures noise from the high-frequency region. For successful continuous-time system identification, selecting appropriate weights on the different spectral components is essential [37], [40]. To automate the spectral component selection, we introduce a weighting matrix in which only diagonal elements are non-zero. This weighting matrix $\mathbf{W}$ is chosen such that there is an emphasis on the significant spectral components. Hence, there is a balance between filtering out the noise and capturing the signal. We take all the off-diagonal elements of the weighting matrix as zeros and set all diagonal elements of the matrix using Kaiser windows of appropriate shapes. We specifically use this window function as the shape of the window can be changed only by changing the parameter $\beta$. This way, we can select the significant spectral components by optimizing over only one parameter $\beta$. A $P$ point Kaiser window function $w_\beta[j]$ can be defined as follows,

$$w_\beta[j] = \begin{cases} \frac{I_0\left(\beta\sqrt{1-\left(\frac{2j}{P-1}-1\right)^2}\right)}{I_0(\beta)}, & 0 \le j \le P-1 \\ 0, & \text{otherwise} \end{cases} \tag{18}$$

where $I_0$ is the zeroth-order modified Bessel function of the first kind $\beta$ determines the shape of the Kaiser window. In this study, we take $P = 2\mathcal{M} + 1$. The optimization formulation (17) can be minimized using $\beta$ values that set matrix $\mathbf{W}(\beta)$ to zero or values close to zero; however, this is not desired. To avoid such situations in estimating $\beta$, we write the time domain equivalent of the optimization formulation (17). Let $\hat{\mathbf{\Theta}} = \underset{\Theta}{\text{argmin}}\, J(\mathbf{\Theta}, \mathbf{u}, \beta) \triangleq f_{\mathbf{u}}(\beta)$. Using (7), $\tau = g(\hat{\mathbf{\Theta}}) = g(f_{\mathbf{u}}(\beta)) \triangleq h(\beta)$. Hence, $\mathbf{A}_\tau \triangleq \mathbf{A}_{h(\beta)}$ and $\mathbf{B}_\tau \triangleq \mathbf{B}_{h(\beta)}$. Using (5), the time domain equivalent of the optimization formulation (17) becomes:

$$\begin{aligned} \underset{\mathbf{\Theta},\mathbf{u},\beta}{\text{minimize}} \quad & \frac{1}{2}||\mathbf{y} - \mathbf{A}_{h(\beta)}y_0 - \mathbf{B}_{h(\beta)}\mathbf{u}||_2^2 \\ \text{subject to} \quad & G(\mathbf{\Theta}) \le \mathbf{0} \\ & ||\mathbf{u}||_0 \ll N \\ & \mathbf{u} \ge \mathbf{0}. \end{aligned} \tag{19}$$

Given $\hat{\mathbf{\Theta}}$ and $\mathbf{u}$, we can find $\beta$ by the optimization problem in (19). We solve this optimization problem using the interior point method.

*2) Sparse Inverse Problem in Hartley Modulating Function Domain:* The optimization problem in (17) is generally considered as NP-hard. An $l_1$-norm relaxation can be used to solve this problem using different techniques including the basis pursuit, greedy algorithms, iterative-thresholding algorithms, or the FOCUSS algorithm and its extensions [41]. We can cast the optimization problem in (17) as,

$$\begin{aligned} \underset{\mathbf{\Theta},\mathbf{u},\beta}{\text{minimize}} \quad & J(\mathbf{\Theta}, \mathbf{u}, \beta) = \frac{1}{2}\boldsymbol{\varepsilon}^\top(\mathcal{M}\omega_0)\mathbf{W}(\beta)\boldsymbol{\varepsilon}(\mathcal{M}\omega_0) + \lambda||\mathbf{u}||_p^p \\ \text{subject to} \quad & G(\mathbf{\Theta}) \le \mathbf{0} \\ & \mathbf{u} \ge \mathbf{0} \end{aligned} \tag{20}$$

where the $l_p$-norm is an approximation to the $l_0$-norm and $\lambda$ is the regularization parameter which determines the sparsity level of the solution for $\mathbf{u}$. FOCUSS algorithm uses a reweighted norm minimization approach to solve the optimization problem while finding stimuli $\mathbf{u}$. By minimizing the $l_2$-norm and refining the initial estimate to the final localized energy solution at each iteration, the solution is obtained [27]. By updating $\lambda$ and $\mathbf{u}$ in every iteration until convergence, we can solve for the sparse vector $\mathbf{u}$. Here, $\lambda$ balances between the sparsity of $\mathbf{u}$ and the weighted residual error $\sqrt{\boldsymbol{W}}\boldsymbol{\varepsilon}$. By increasing the value of $\lambda$, $\mathbf{u}$ becomes more sparse. The matrix $\boldsymbol{B}_{\boldsymbol{\phi}}^\top(\mathcal{M}\omega_0)$ is the same in every step and can be calculated only once at the beginning of the algorithm. This makes the algorithm more efficient.

To ensure there is a balance between filtering out the noise and capturing the sparsity of the input, we use the Generalized Cross-Validation (GCV) technique [42] for estimating the regularization parameter. Hence, we use a modified version of the FOCUSS algorithm called GCV-FOCUSS+ [25] algorithm, which is based on the FOCUSS+ [41] and includes a GCV step. A detail description of FOCUSS+ and GCV-FOCUSS+ algorithms is given in supplementary information.

Algorithm 1 summarizes the system identification approach using Hartley modulating functions.

**Algorithm 1**: Hartley Modulating Function-Based Continuous System Identification with Adaptive Band Selection

*Part A:*

**(a)** Calculate the maximum bandwidth $\omega_{max}$ of the system using (6) and the $\tau_1^{max}$ and $\tau_2^{max}$.

**(b)** $\mathcal{M} = \frac{2\omega_{max}}{\omega_0}$.

**(c)** Find all HMF spectral components for $m \in \{-\mathcal{M}, -\mathcal{M}+1, \cdots, -2, -1, 0, 1, 2, \cdots, \mathcal{M}-1, \mathcal{M}\}$.

**(d)** Initialize $\mathbf{\Theta}_{(0)}$ and $\beta_{(0)}$ using the initialization algorithm described in the supplementary information.

*Part B:*

**(e)** Let $j = 0$.

**(f)** Set $j = j + 1$.

**(g)** Set $\mathbf{u}$ and $\mathbf{\Theta}$ equal to $\hat{\mathbf{u}}$ and $\mathbf{\Theta}_{(j-1)}$, respectively and solve for $\beta_{(j)}$ by initializing optimization formulation in (19) at $\beta_{(j-1)}$.

**(h)** Set $\mathbf{u}$ and $\beta$ equal to $\hat{\mathbf{u}}$ and $\beta_{(j)}$, respectively and solve for $\mathbf{\Theta}_{(j)}$ by initializing optimization formulation in (17) at $\mathbf{\Theta}_{(j-1)}$.

**(i)** Iterate between (f)-(h) until convergence.

*3) Coordinate Descent Deconvolution:* In the coordinate descent approach, first, we filter the signal using a 0.5 Hz 64 order FIR lowpass filter [43]. Then, we use cvxEDA method [23] to separate the phasic component from filtered SC data. By combining the methods described in Sections II-C2 and II-C1, a coordinate descent approach can be implemented. Before performing deconvolution, we initialize the algorithm by sampling the system parameters from uniform distributions within the boundary conditions. The detailed description of the initialization algorithm is provided in the supplementary information. We propose the following algorithm to recover $\mathbf{u}$ and $\mathbf{\Theta}$ from the phasic component.

**Algorithm 2**: Coordinate Descent in Hartley Modulating Function Domain

**(a)** Let i = 0.

**(b)** Run Algorithm 1-A.

**(c)** Set i = i + 1.

**(d)** Initialize $\hat{\mathbf{u}}^0$ using the initialization algorithm described in the supplementary information.

**(e)** Set $\mathbf{\Theta}$ and $\beta$ equal to $\hat{\mathbf{\Theta}}^{(i-1)}$ and $\hat{\beta}^{(i-1)}$; solve for $\hat{\mathbf{u}}^i$ using GCV-FOCUSS+ by initializing the inverse problem in (20) at $\hat{\mathbf{u}}^{(i-1)}$.

**(f)** Set $\mathbf{u}$ equal to $\hat{\mathbf{u}}^{(i)}$; to solve for $\hat{\mathbf{\Theta}}^{(i)}$ and $\hat{\beta}^{(i)}$ using Algorithm 1-B by initializing $\mathbf{\Theta}_{(0)}$ and $\beta_{(0)}$ at $\hat{\mathbf{\Theta}}^{(i-1)}$ and $\hat{\beta}^{(i-1)}$, respectively.

**(g)** Iterate between (c)-(f) until convergence.

We run Algorithm 2 for several uniform random initializations

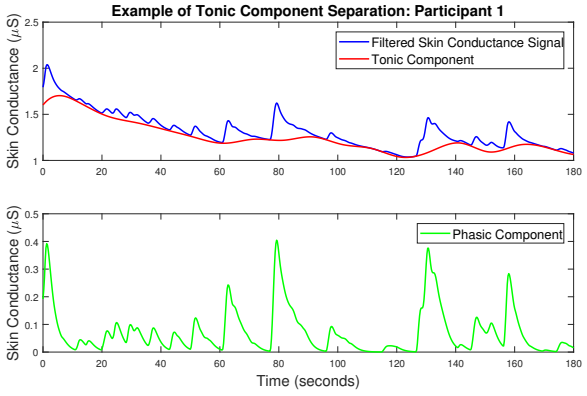


Fig. 1: **Tonic Component Separation Example.** i) The top panel shows the lowpass filtered SC signal (blue curve) and the corresponding estimated tonic part (red curve) with cvxEDA algorithm [23]. ii) The bottom panel shows the extracted phasic component for the corresponding SC signal after subtracting the tonic part.

of $\mathbf{\Theta}$ and take the solution of $\hat{\mathbf{u}}$ and $\hat{\mathbf{\Theta}}$ (Setting $\tau = \mathbf{g}(\mathbf{\Theta})$) that provides the smallest value of $||\mathbf{y} - \mathbf{A}_\tau y_0 - B_\tau \mathbf{u}||_2^2$. The recovered neural stimuli in the HMF domain can sometimes lead to lower amplitudes for impulses that occur in the beginning or at the end of the neural stimuli vector $\mathbf{u}$. Hence, to ensure this type of behavior does not occur, using the estimated $\hat{\tau}$, in the time domain (similar to [20], [19]), we run the FOCUSS+ algorithm one last time by initializing $\mathbf{u}$ at a vector of all ones and considering a maximum sparsity equal to $||\hat{\mathbf{u}}||_0$.

TABLE I: Results from Experimental Data

| Participant | $\tau_1$ (seconds) | $\tau_2$ (seconds) | $R^2$ | $N_u$ | $\lambda$ |
|---|---|---|---|---|---|
| 1 | 1.231 | 2.665 | 0.973 | 23 | $1.10 \times 10^{-3}$ |
| 2 | 0.512 | 2.958 | 0.966 | 28 | $1.80 \times 10^{-3}$ |
| 3 | 0.414 | 3.163 | 0.963 | 17 | $2.90 \times 10^{-3}$ |
| 4 | 0.237 | 4.849 | 0.916 | 15 | $2.60 \times 10^{-3}$ |
| 5 | 0.783 | 3.367 | 0.971 | 44 | $3.62 \times 10^{-2}$ |
| 6 | 0.362 | 3.362 | 0.927 | 40 | $1.00 \times 10^{-3}$ |

The parameters $\tau_1$ and $\tau_2$ are the estimated rise time and fall time of the phasic SC, respectively. $N_u$ is the estimated number of neural stimuli impulses from ANS and $R^2$ is the square of the multiple correlation coefficient.

## III. Results

Figure 1 shows an example of the tonic component separation with cvxEDA algorithm [23]. Figure 2 shows the phasic component, recovered neural stimuli, and the reconstructed phasic component of the SC data collected for the participants from Dataset 1. There are several SC peaks present in the data which correspond to the cognitive stress originating from the 'counting task'. Figure 2 also shows the recovered neural stimuli timings and amplitudes that correspond to cognitive stress. Reconstructed signals in Figure 2 were generated using the model defined in (1)-(2). Table I shows the corresponding estimated rise time $\tau_1$ and decay time $\tau_2$. In Table II, all the multiple correlation coefficients ($R^2$) are over 0.915. Table I also shows the regularization parameter $\lambda$ obtained using GCV. All the regularization parameters are less than $3.7 \times 10^{-2}$ with minimum value of $1 \times 10^{-3}$. Quantile-quantile plots of the residuals after reconstruction follows a straight line, which implies the residuals are zero-mean Gaussian distributed (as assumed in the problem formulation). The quantile-quantile plots are provided in the supplementary information. Figures of the SC reconstructed signals with both tonic and phasic components are also provided in the supplementary information. The values $R^2$ for this case is higher than 0.95 for all of the participants if calculated considering both tonic and phasic components.

We have simulated noisy phasic SC data using results in Table I and Figure 2, and then performed deconvolution on simulated data to further validate our algorithm. For simulated data, both the sparse input and the model parameters are known, and we can compare the deconvolution results with the ground truth. To simulate the noise, we take zero-mean Gaussian random variables with 25 dB signal to noise ratio (SNR) for each participant. Figure 3 shows the recovered amplitudes and timings of the impulses for the simulated phasic SC data. Table II shows results obtained from the simulated data. The multiple correlation coefficients ($R^2$) are above 0.97 for noisy simulated data. Blue impulses in Figure 3 are the ground truth impulses used for simulating the data.

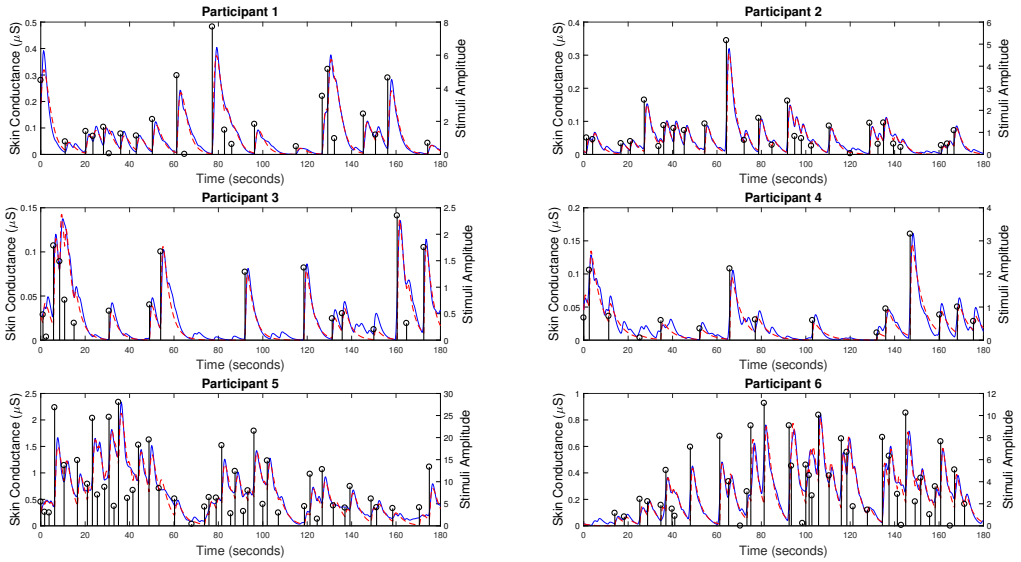


Fig. 2: **Estimated Deconvolution of the Experimental Phasic SC Data in 6 Participants from Dataset 1.** Each panel shows the separated phasic component of the SC data using cvxEDA (blue curve), the estimated reconstructed signal (red dashed), the estimated neural stimuli timings and amplitudes (black vertical lines with the circle on top) for each of the participants.

TABLE II: Results from Simulated Data

| Participant | $\tau_1$ (seconds) | $\tau_2$ (seconds) | $\hat{\tau}_1$ | $\hat{\tau}_2$ | $R^2$ | $\hat{N}_u$ | $\lvert N - \hat{N}_u \rvert$ | $\frac{\lvert\tau_1-\hat{\tau}_1\rvert}{\tau_1} \times 100$ % | $\frac{\lvert\tau_2-\hat{\tau}_2\rvert}{\tau_2} \times 100$ % |
|---|---|---|---|---|---|---|---|---|---|
| 1 | 1.231 | 2.665 | 1.167 | 2.726 | 0.989 | 21 | 2 | 5.20 | 2.29 |
| 2 | 0.512 | 2.958 | 0.389 | 3.349 | 0.977 | 24 | 4 | 24.02 | 13.22 |
| 3 | 0.414 | 3.163 | 0.456 | 3.074 | 0.974 | 14 | 3 | 10.14 | 2.81 |
| 4 | 0.237 | 4.849 | 0.182 | 4.906 | 0.985 | 14 | 1 | 23.21 | 1.18 |
| 5 | 0.783 | 3.367 | 0.727 | 3.352 | 0.987 | 44 | 0 | 7.15 | 4.09 |
| 6 | 0.362 | 3.369 | 0.311 | 3.345 | 0.984 | 36 | 4 | 14.09 | 0.71 |

The parameters $\hat{\tau}_1$ and $\hat{\tau}_2$ are, respectively, the estimated rise time and decay time of phasic SC. $\hat{N}_u$ is the estimated number of neural stimuli impulses from ANS and $R^2$ is the square of the multiple correlation coefficient. Zero mean Gaussian noise has been added to each simulated data point compared to each of the simulated signal. The noise SNR is 25 dB for all of the simulated data. For each participant, the variance of noise is calculated by taking the variance of the residuals after deconvolution on real data. The parameters $\tau_1$ and $\tau_2$ are, respectively, the rise time and decay time of phasic SC used for simulating each dataset. The values of $\tau_1$ and $\tau_2$ are given in Table I.

Figure 3 illustrates that all the significant impulses have been detected. However, some of the very small impulses were missed in presence of noise. The amplitudes and timings of the detected neural stimuli are very close to the ground truth.

Table II shows the detected rise and fall times along with the percentage errors. All the percentage errors are below 25%. The maximum error in detecting the number of impulses in the neural stimuli is 4. For simulated data based on participants 2 and 6, the algorithm has missed 4 of the impulses that are insignificant and comparable to the level of added noise. However, the algorithm has detected all of the significant impulses.

We also analyze SC data from one male participant (subject ID 11) and one female participant (subject ID 15) from Dataset 2. Dataset 2 has auditory stimulation timings information to perform the comparison with the recovered neural stimuli. We expect to see a time delay from the auditory stimulation to the neural stimuli as the neural system should take some time to generate neural stimuli after an auditory stimulation has occurred. Figure 4 shows our approach detects an impulse after every auditory stimulation. The average delays are 2.02 seconds for the male participant and 2.08 seconds for the female participant. The rise time and the decay time for the male participant are 0.34 seconds and 3.41 seconds, respectively. For the female participant, the time constants are 0.59 seconds and 3.32 seconds, respectively. We also compare this performance with other approaches. The LedaLab [22] and the cvxEDA [23] algorithms detect too many pulses compared to our approach.

To further compare the performance of our algorithm with the existing algorithms, we used a synthetic $u(t)$ to simulate data using the model in (1)-(2) with model parameters $\boldsymbol{\tau} = \begin{bmatrix} 0.7 & 4.0 \end{bmatrix}$ and noise level of 20 dB signal SNR. Figure 5 (a) and Figure 5 (b) show the synthetic neural stimuli and the simulated data, respectively. We then apply different algorithms to compare the performance. Figure 5 shows the performances of different algorithms. In this case, we assume $\tau_1$ and $\tau_2$ are known because the existing algorithms only solve the inverse problem and do not perform deonvolution. Figure 5 (c) shows that LedaLab [22] detects too many

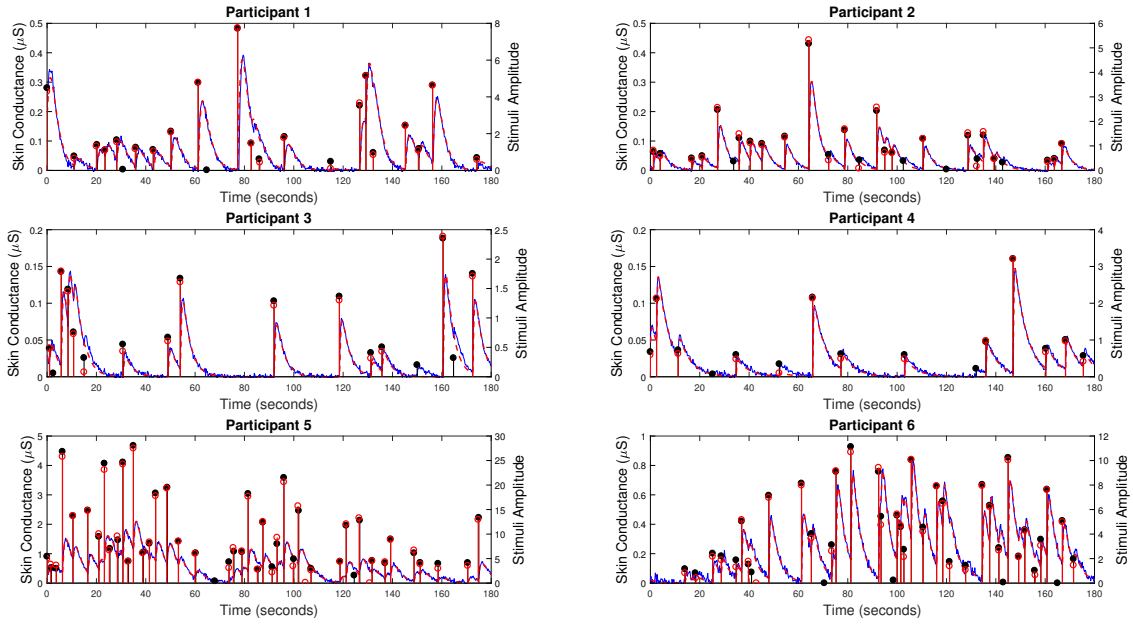


Fig. 3: **Estimated Neural Stimuli and Reconstructed Signals of the Simulated Phasic SC Data with 25 dB SNR in 6 Participants from Dataset 1.** Each panel shows the simulated phasic component of the SC data (blue curve), the estimated reconstructed signal (red dashed), the estimated neural stimuli timings and amplitudes (red vertical lines with the circle on top) and the ground truth of the neural stimuli timings and amplitudes for each of the simulated data (black lines with the dots on top).

impulses compared to the ground truth. Figure 5 (d) shows that cvxEDA [23] detects a more sparse solution compared to Ledalab; however, it still detects too many impulses compared to the ground truth. As observed, our result in Figure 5 (e) outperforms the existing algorithms.

We also compare the performance of our algorithm with the deconvolution algorithm proposed in [20], [19]. Figure 6 shows the result obtained from simulated data using coordinate descent approach for estimating unknowns $\tau_1$, $\tau_2$ and $\mathbf{u}$. Figure 6 (a) shows the result with interior point method as in [20], [19] and Figure 6 (b) shows the result with proposed HMF domain method. The estimated rise time and fall time using the proposed method are 0.7054 seconds and 3.9726 seconds, respectively. For both of them, the estimation error is less than 1%. Whereas, the estimated rise time and fall time using the time domain interior point based coordinate algorithm are 0.5562 seconds and 4.2501 seconds, respectively. In this case, errors are 20.5408% and 6.2514%, receptively. The proposed algorithm has outperforms than the time domain approach. In this study, we used 16 random initialization for both algorithms.

## IV. Discussions

Finding the neural stimuli and physiological system parameters related to SC is a challenging problem. Firstly, there can exist multiple sets of physiological parameters and stimuli that closely approximate an observed signal. Secondly, the smallest level of noise can perturb the solution to a physiologically infeasible point due to the sensitive nature of the bi-exponential function. To overcome these challenges, proper boundary conditions and constraints have to be applied in the optimization problem. Alexander *et al.* [31], use the values of $\tau_1 = 0.75$ seconds and $\tau_2 = 2$ seconds for all datasets they have analyzed. Greco *et al.* [23] set $\tau_1 = 0.75$ and use fixed $\tau_2$ values that vary between 2 and 4. We assume that the rise times lie between 0.10 to 1.40 seconds to have more flexibility to the subject-specific variations. We also assume decay times are between 1.5 and 6 seconds, respectively. To impose the constraints on $\boldsymbol{\tau}$ during continuous system identification using Hartley modulating function, we used 5 nonlinear physiological constraints on $\alpha_1$ and $\alpha_2$ to ensure identifiability. Table I shows the corresponding estimated rise times $\tau_1$ and decay times $\tau_2$ which lie within the boundary. The boundary constraints have been chosen such that the system is identifiable and the model parameters do not stagnate at the boundaries.

A good separation of the tonic component depends on an appropriate choice of smoothness of the tonic component which is enforced by the selection of the basis for the tonic component and the $l_2$ -norm penalization parameter of the spline coefficients in cvxEDA [23]. In this study, we follow cvxEDA [23] for obtaining the tonic component. While cvxEDA [23] has good performance in separating the tonic component from the signal, it can overfit the noise in the phasic component. Moreover, instead of including the subject-specific rise and decay times, it assumes these values are fixed. Taking the phasic component, we use our deconvolution approach to estimate the rise and decay times as well as the stimuli while

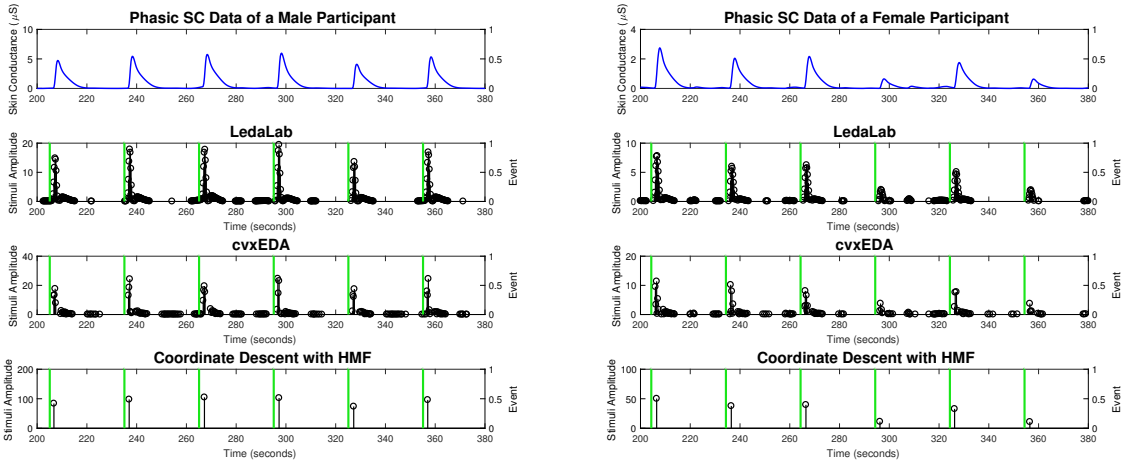


Fig. 4: **Estimated Neural Stimuli from the Experimental Phasic SC Data in two Participants from Dataset 2.** i) The top sub-panels show the separated phasic component of the SC data (blue curve), ii) second sub-panels depict the estimated neural stimuli with ledaLab [22] (black vertical lines), iii) third sub-panels show the estimated neural stimuli with cvxEDA [23] algorithm (black vertical lines), vi) last sub-panels show the estimated neural stimuli with the proposed approach (black vertical lines). Green vertical lines represent the timings of the auditory stimulations.

filtering out the noise. To obtain the phasic component in this study, we used the default parameters in cvxEDA [23]. The value of these parameters is crucial for good separation of the tonic and phasic components.

An inappropriate choice of the input sparsity level ($\mathbf{u}$) and minimum separation constraint between the input impulses (arrival time in $\mathbf{u}$) can lead to an incorrect solution. While the higher number of impulses can lead to overfitting (i.e. capturing the noise as impulse), higher sparsity level may fail to recover the underlying process. In the initialization step, we choose a minimum separation of 0.5 seconds for the arrival time of the impulses in the FOCUSS+ algorithm. In the coordinate descent step, GCV-FOCUSS+ provides a balance in sparsity of the stimuli such that it captures the process yet filters out most of the noise.

Table I shows the regularization parameters from the GCV-FOCUSS+ part of the algorithm. We constrained $\lambda$ between 0 and 0.1. The choice of the regularization parameters $\lambda$ depends on the subject-specific magnitude of the SC signal. The results from the simulated data based on participants 3, 4 and 6 show that in some cases if there are many small adjacent impulses present in the stimuli in presence of high levels of noise, some of these small impulses in stimuli might be missed by the proposed deconvolution algorithm. In this case, the GCV-FOCUSS+ part of the algorithm considers these small spikes as noise. As a consequence, the estimation of rise time could become inaccurate. The decay times are larger in magnitude and are less affected. The deconvolution algorithm always recovers the significant impulses in the stimuli successfully.

The optimization step for finding the stimuli in II-C2 is a convex problem [41]. In this study, we formulate an optimization problem that is convex in terms of system parameters and neural stimuli. The proof provided in the appendix shows the convexity of the problem formulation in terms of $\mathbf{\Theta}$ and $\mathbf{u}$. However, one should note that in implementing the GCV-FOCUSS+ algorithm, if an impulse goes to zero, it never becomes non-zero in the next iterations of the coordinate descent approach. Hence, sometimes the algorithm might not reach the global minimum depending on the initial condition. Moreover, the optimization problem formulation is not convex in terms of $\beta$. As a result, it is still possible to stagnate at a local minimum using this approach. We used several random initializations within the boundary conditions to account for this.

Wickramasuriya et al. [44] used the dataset in [28] (discussed in II-A) and recovered the stimuli using cvxEDA [23]. Then, they used a heuristic approach to obtain a more sparse neural stimuli. Then, they used these sparse neural stimuli for tracking stress [44]. Our proposed algorithm provides an appropriate sparsity level and can be used directly to track stress using the approach in [44].

## V. Conclusion and Future Works

SC depends on the thermal regulation of the body as well as the sympathetic nervous activity. SC can be a means of understanding emotional disorders and abnormalities. Monitoring emotional states and understanding these disorders and abnormalities will enable patients to receive necessary actions or treatment for better mental health. To obtain emotional information from SC, recovering system parameters and the underlying neural stimuli is necessary. We use cvxEDA to separate the phasic component of SC data, and then perform deconvolution to recover the underlying neural stimuli. We model the phasic component of the signal using a state-space model similar to the models in [31], [19], [20]. [19], [20]. Then, we propose a two-step coordinate descent deconvolution scheme to identify the system parameters and the underlying neural stimuli. We use a system identification approach that

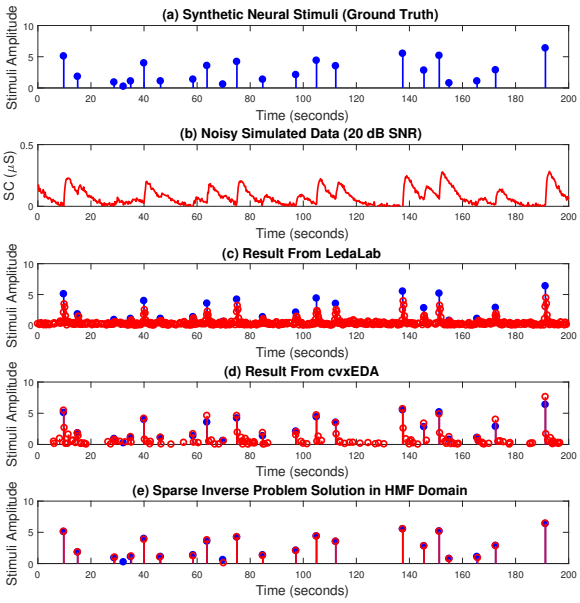


Fig. 5: **Comparison of Different Sparse Recovery Algorithms with Simulated Data.** (a) A synthetic neural stimuli (ground truth). (b) Simulated data with $\tau_1 = 0.7$ seconds, $\tau_2 = 4$ seconds and synthetic neural stimuli $u(t)$ with added noise of 20 dB SNR. (c) The solutions from LedaLab [22], (d) the solution from cvxEDA [23] and (e) the sparse inverse problem solution in HMF domain [20]. Blue line, red line, and red curve correspond to ground truth, estimated stimuli and simulated data, respectively.

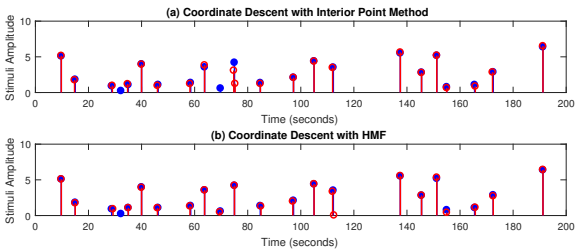


Fig. 6: **Comparison of Two Deconvolution Algorithms using Simulated Data.** Coordinate descent simulated data deconvolution results using (a) interior point method and (b) HMF method. Blue lines, red lines, and red curve correspond to ground truth, estimated stimuli and simulated data, respectively. The result is obtained from the simulated data in Figure 5 (a)

recovers the system parameters and neural stimuli in the HMF domain. We incorporate an adaptive band selection scheme in HMF domain to have the best possible estimate. We also use GCV-FOCUSS+ to solve the inverse problem and find the neural stimuli in HMF domain. We apply our algorithm to analyze the SC data collected from subjects who were performing tasks involving 'cognitive stress'. Finally, to validate our algorithm, we simulate noisy data based on the results obtained from the deconvolution of experimental data. We illustrate that our algorithms successfully deconvolves noisy simulated data. We also compare performance of our method with cvxEDA [23] and LedaLab [22] algorithms. Our algorithm outperforms both these algorithms in finding the stimuli while balancing between the sparsity and filtering out the noise. Moreover, our algorithm estimates the system parameters while the other two algorithms assume fixed known system parameters.

Using the output of this deconvolution approach, we plan to formulate a state-space framework for estimating one's internal emotional states. Furthermore, we plan to extend this approach to deconvolution of different pulsatile hormones.

## REFERENCES


[1] D. C. Fowles, M. J. Christie, R. Edelberg, W. W. Grings, D. T. Lykken, and P. H. Venables, "Publication recommendations for electrodermal measurements," *Psychophysiology*, vol. 18, no. 3, pp. 232–239, 1981.

[2] J. L. Andreassi, *Psychophysiology: Human behavior & physiological response*. Psychology Press, 2013.

[3] M. E. Dawson, A. M. Schell, and D. L. Filion, "The electrodermal system," *Handbook of psychophysiology*, vol. 2, pp. 200–223, 2007.

[4] H. D. Critchley, "Electrodermal responses: what happens in the brain," *The Neuroscientist*, vol. 8, no. 2, pp. 132–142, 2002.

[5] N. A. Groenewold, E. M. Opmeer, P. de Jonge, A. Aleman, and S. G. Costafreda, "Emotional valence modulates brain functional abnormalities in depression: evidence from a meta-analysis of fmri studies," *Neuroscience & Biobehavioral Reviews*, vol. 37, no. 2, pp. 152–163, 2013.

[6] K. Hawton, C. C. i Comabella, C. Haw, and K. Saunders, "Risk factors for suicide in individuals with depression: a systematic review," *Journal of affective disorders*, vol. 147, no. 1, pp. 17–28, 2013.

[7] M. Beghi, J. F. Rosenbaum, C. Cerri, and C. M. Cornaggia, "Risk factors for fatal and nonfatal repetition of suicide attempts: a literature review," *Neuropsychiatric disease and treatment*, vol. 9, p. 1725, 2013.

[8] M. Pompili, L. Sher, G. Serafini, A. Forte, M. Innamorati, G. Dominici, D. Lester, M. Amore, and P. Girardi, "Posttraumatic stress disorder and suicide risk among veterans: a literature review," *The Journal of nervous and mental disease*, vol. 201, no. 9, pp. 802–812, 2013.

[9] E. R. Walker, R. E. McGee, and B. G. Druss, "Mortality in mental disorders and global disease burden implications: a systematic review and meta-analysis," *JAMA psychiatry*, vol. 72, no. 4, pp. 334–341, 2015.

[10] K.-i. Yamamoto, T. Shinba, and M. Yoshii, "Psychiatric symptoms of noradrenergic dysfunction: a pathophysiological view," *Psychiatry and clinical neurosciences*, vol. 68, no. 1, pp. 1–20, 2014.

[11] K. C. Peterson, M. F. Prout, and R. A. Schwarz, *Post-traumatic stress disorder: A clinicianâĂŹs guide*. Springer Science & Business Media, 2013.

[12] J. J. Gross and H. Jazaieri, "Emotion, emotion regulation, and psychopathology: An affective science perspective," *Clinical Psychological Science*, vol. 2, no. 4, pp. 387–401, 2014.

[13] K. Werner and J. J. Gross, "Emotion regulation and psychopathology: A conceptual framework." 2010.

[14] V. G. Macefield, C. James, and L. A. Henderson, "Identification of sites of sympathetic outflow at rest and during emotional arousal: concurrent recordings of sympathetic nerve activity and fmri of the brain," *International Journal of Psychophysiology*, vol. 89, no. 3, pp. 451–459, 2013.

[15] U. Hegerl, C. Sander, and T. Hensch, "Arousal regulation in affective disorders," *Systems neuroscience in depression*, pp. 341–370, 2016.

[16] D. Zhou, J. Luo, V. M. Silenzio, Y. Zhou, J. Hu, G. Currier, and H. A. Kautz, "Tackling mental health by integrating unobtrusive multimodal sensing." in *AAAI*, 2015, pp. 1401–1409.

[17] M. Bomba, F. Corbetta, A. Gambera, F. Nicosia, L. Bonini, F. Neri, L. Tremolizzo, and R. Nacinovich, "Heart rate variability in adolescents with functional hypothalamic amenorrhea and anorexia nervosa," *Psychiatry research*, vol. 215, no. 2, pp. 406–409, 2014.

[18] P. J. Soh, G. A. Vandenbosch, M. Mercuri, and D. M.-P. Schreurs, "Wearable wireless health monitoring: Current developments, challenges, and future trends," *IEEE Microwave Magazine*, vol. 16, no. 4, pp. 55–70, 2015.

[19] R. T. Faghih, P. A. Stokes, M.-F. Marin, R. G. Zsido, S. Zorowitz, B. L. Rosenbaum, H. Song, M. R. Milad, D. D. Dougherty, E. N. Eskandar *et al.*, "Characterization of fear conditioning and fear extinction by analysis of electrodermal activity," in *Engineering in Medicine and Biology Society (EMBC), 2015 37th Annual International Conference of the IEEE*. IEEE, 2015, pp. 7814–7818.

[20] R. T. Faghih, M. A. Dahleh, G. K. Adler, E. B. Klerman, and E. N. Brown, "Deconvolution of serum cortisol levels by using compressed sensing," *PloS one*, vol. 9, no. 1, p. e85204, 2014.

[21] R. T. Faghih, M. A. Dahleh, G. K. Adler, E. B. Klerman, and E. N. Brown, "Quantifying pituitary-adrenal dynamics and deconvolution of concurrent cortisol and adrenocorticotropic hormone data by compressed sensing," *IEEE Transactions on Biomedical Engineering*, vol. 62, no. 10, pp. 2379–2388, 2015.

[22] M. Benedek and C. Kaernbach, "Decomposition of skin conductance data by means of nonnegative deconvolution," *Psychophysiology*, vol. 47, no. 4, pp. 647–658, 2010.

[23] A. Greco, G. Valenza, A. Lanata, E. P. Scilingo, and L. Citi, "cvxeda: A convex optimization approach to electrodermal activity processing," *IEEE Transactions on Biomedical Engineering*, vol. 63, no. 4, pp. 797–804, 2016.

[24] F. Hernando-Gallego, D. Luengo, and A. Artés-Rodríguez, "Feature extraction of galvanic skin responses by non-negative sparse deconvolution," *IEEE Journal of Biomedical and Health Informatics*, 2017.

[25] R. T. Faghih, "System identification of cortisol secretion: Characterizing pulsatile dynamics," Ph.D. dissertation, Massachusetts Institute of Technology, 2014.

[26] R. T. Faghih, "From physiological signals to pulsatile dynamics: a sparse system identification approach," in *Dynamic Neuroscience*. Springer, 2018, pp. 239–265.

[27] I. F. Gorodnitsky and B. D. Rao, "Sparse signal reconstruction from limited data using focuss: A re-weighted minimum norm algorithm," *IEEE Transactions on signal processing*, vol. 45, no. 3, pp. 600–616, 1997.

[28] J. Birjandtalab, D. Cogan, M. B. Pouyan, and M. Nourani, "A non-eeg biosignals dataset for assessment and visualization of neurological status," in *Signal Processing Systems (SiPS), 2016 IEEE International Workshop on*. IEEE, 2016, pp. 110–114.

[29] D. R. Bach, G. Flandin, K. J. Friston, and R. J. Dolan, "PsPM-SCRV10: Skin conductance responses to loud sounds, simultanously recorded from palm, fingers and foot," Feb. 2017. [Online]. Available: https://doi.org/10.5281/zenodo.291465

[30] D. R. Bach, G. Flandin, K. J. Friston, and R. J. Dolan, "Modelling event-related skin conductance responses," *International Journal of Psychophysiology*, vol. 75, no. 3, pp. 349–356, 2010.

[31] D. M. Alexander, C. Trengove, P. Johnston, T. Cooper, J. August, and E. Gordon, "Separating individual skin conductance responses in a short interstimulus-interval paradigm," *Journal of neuroscience methods*, vol. 146, no. 1, pp. 116–123, 2005.

[32] S. Jain, U. Oswal, K. S. Xu, B. Eriksson, and J. Haupt, "A compressed sensing based decomposition of electrodermal activity signals," *IEEE Transactions on Biomedical Engineering*, vol. 64, no. 9, pp. 2142–2151, 2017.

[33] H. Preisig and D. Rippin, "Theory and application of the modulating function methodâĂŤi. review and theory of the method and theory of the spline-type modulating functions," *Computers & chemical engineering*, vol. 17, no. 1, pp. 1–16, 1993.

[34] G. Rao and H. Unbehauen, "Identification of continuous-time systems," *IEE Proceedings-Control theory and applications*, vol. 153, no. 2, pp. 185–220, 2006.

[35] A. PATRA and H. UNBEHAUEN, "Identification of a class of nonlinear continuous-time systems using hartley modulating functions," *International Journal of Control*, vol. 62, no. 6, pp. 1431–1451, 1995.

[36] H. Unbehauen and P. Rao, "Identification of continuous-time systems: A tutorial," *IFAC Proceedings Volumes*, vol. 30, no. 11, pp. 973–999, 1997.

[37] S. Daniel-Berhe and H. Unbehauen, "Bilinear continuous-time systems identification via hartley-based modulating functions," *Automatica*, vol. 34, no. 4, pp. 499–503, 1998.

[38] R. N. Bracewell, *The hartley transform*. Oxford University Press, Inc., 1986.

[39] H. Garnier, M. Mensler, and A. Richard, "Continuous-time model identification from sampled data: implementation issues and performance evaluation," *International journal of Control*, vol. 76, no. 13, pp. 1337–1357, 2003.

[40] A. Pearson, "Explicit parameter identification for a class of nonlinear input/output differential operator models," in *Decision and Control, 1992., Proceedings of the 31st IEEE Conference on*. IEEE, 1992, pp. 3656–3660.

[41] J. F. Murray, "Visual recognition, inference and coding using learned sparse overcomplete representations," Ph.D. dissertation, University of California, San Diego, 2005.

[42] G. H. Golub, M. Heath, and G. Wahba, "Generalized cross-validation as a method for choosing a good ridge parameter," *Technometrics*, vol. 21, no. 2, pp. 215–223, 1979.

[43] A. Sano, A. J. Phillips, Z. Y. Amy, A. W. McHill, S. Taylor, N. Jaques, C. A. Czeisler, E. B. Klerman, and R. W. Picard, "Recognizing academic performance, sleep quality, stress level, and mental health using personality traits, wearable sensors and mobile phones," in *Wearable and Implantable Body Sensor Networks (BSN), 2015 IEEE 12th International Conference on*. IEEE, 2015, pp. 1–6.

[44] D. Wickramasuriya, C. Qi, and R. T. Faghih, "A state-space approach for detecting stress from electrodermal activity," in *Engineering in Medicine and Biology Society (EMBC), 2018 40th Annual International Conference of the IEEE*. IEEE, 2018.


## Appendix A
## Proof of Convexity of The HMF based Cost Function

The optimization formulation (17) is jointly convex in $\mathbf{u}$ and $\Theta$. It can be shown that (17) satisfies first-order and second-order convexity condition.

**First-order convexity condition**

Let $\chi_i = \begin{bmatrix} \Theta_i^\top & \mathbf{u}_i^\top \end{bmatrix}^\top$ and $A_\phi = \begin{bmatrix} \mathbf{\Phi} & \boldsymbol{B}_\phi \end{bmatrix}$. The cost function in (17) can be rewritten as,

$$J(\chi_i) = \frac{1}{2}\left[\mathbf{Z} - A_\phi \chi_i\right]^\top \mathbf{W}\left[\mathbf{Z} - A_\phi \chi_i\right].$$

$J : \mathbb{R}^{N+2} \rightarrow \mathbb{R}$ is convex if and only if $J(\chi_2) - J(\chi_1) - \nabla J(\chi_1)^\top(\chi_2 - \chi_1) \geq 0$ for any $\chi_1$ and $\chi_2$ in **dom** $J$.

$$\nabla J(\chi_1) = -2A_\phi^\top \mathbf{W}(\zeta - A_\phi \chi_1).$$

Plugging in the value it can be shown that,

$$\begin{aligned} &J(\chi_2) - J(\chi_1) - \nabla J(\chi_1)^\top(\chi_2 - \chi_1) \\ &= (\chi_2 - \chi_1)^\top A_\phi^T \mathbf{W} A_\phi (\chi_2 - \chi_1). \end{aligned} \tag{21}$$

The right hand side of (21) is always positive as $\mathbf{W}$ is positive semidefinite. So $J$ satisfies the first order condition.

**Second-order convexity condition**

Taking the second derivative of $J$,

$$\nabla^2 J(\chi) = A_\phi^\top \mathbf{W} A_\phi.$$

As $\mathbf{W}$ is a positive semidefinite matrix, $\nabla^2 J(\chi) \geq 0$.

The cost function in HMF domain satisfies first and second order conditions of convexity. So, the cost function is jointly convex in $\Theta$ and $\mathbf{u}$.